www.acsnano.org

Dynamic Changes in Heparan Sulfate Nanostructure in Human Pluripotent Stem Cell Differentiation

Deena Al Mahbuba, Sayaka Masuko, Shiwei Wang, Deepsing Syangtan, Jeong Seuk Kang, Yuefan Song, Tay Won Shin, Ke Xia, Fuming Zhang, Robert J. Linhardt, Edward S. Boyden, and Laura L. Kiessling*



Downloaded via VIRGINIA POLYTECH INST STATE UNIV on July 27, 2023 at 17:43:25 (UTC). See https://pubs.acs.org/sharingguidelines for options on how to legitimately share published articles.

Cite This: ACS Nano 2023, 17, 7207-7218



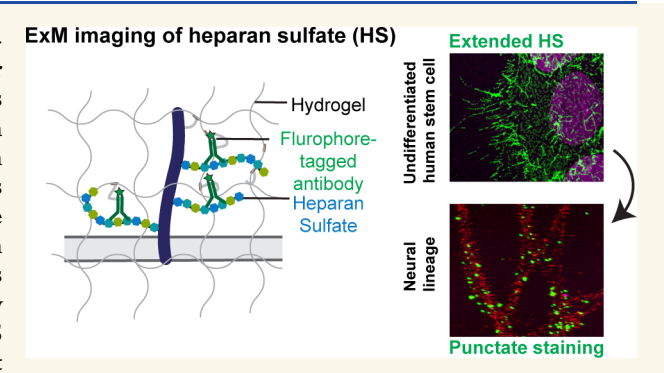
ACCESS I

III Metrics & More

Article Recommendations

Supporting Information

ABSTRACT: Heparan sulfate (HS) is a heterogeneous, cell-surface polysaccharide critical for transducing signals essential for mammalian development. Imaging of signaling proteins has revealed how their localization influences their information transfer. In contrast, the contribution of the spatial distribution and nanostructure of information-rich, signaling polysaccharides like HS is not known. Using expansion microscopy (ExM), we found striking changes in HS nanostructure occur as human pluripotent stem (hPS) cells differentiate, and these changes correlate with growth factor signaling. Our imaging studies show that undifferentiated hPS cells are densely coated with HS displayed as hair-like protrusions. This ultrastructure can recruit fibroblast growth factor for signaling. When the hPS cells



differentiate into the ectoderm lineage, HS is localized into dispersed puncta. This striking change in HS distribution coincides with a decrease in fibroblast growth factor binding to neural cells. While developmental variations in HS sequence were thought to be the primary driver of alterations in HS-mediated growth factor signaling, our high-resolution images indicate a role for the HS nanostructure. Our study highlights the utility of high-resolution glycan imaging using ExM. In the case of HS, we found that changes in how the polysaccharide is displayed link to profound differences in growth factor binding.

KEYWORDS: heparan sulfate, expansion microscopy, glycan nanostructure, human pluripotent stem cells, neuronal differentiation

ammalian cells are covered with a dense layer of carbohydrates. This glycan coat is critical for numerous biological processes, including cell-cell recognition, cancer initiation and progression, and embryonic development. An integral part of this coat's ability to mediate information transfer is the extracellular polysaccharide heparan sulfate (HS), a ubiquitous and critical component of the mammalian glycocalyx. HS is a highly sulfated, polyanionic glycosaminoglycan whose sequence can vary. Distinct HS sequences determine how HS interacts with diverse binding partners, ranging from growth factors to synaptic proteins. Although the chemical composition of purified HS sequences can be used to understand the role of this information-rich glycan, the molecular diversity of HS in its native environment is challenging to probe. Thus, approaches for visualizing endogenous cell-surface complex glycans, such as HS, are needed, especially to elucidate the interplay between their distribution and roles in the signal transduction pathways critical for human development and disease.

Human pluripotent stem (hPS) cells serve as a rich source of information on the mechanisms that underlie human signaling because these cells can self-renew or undergo differentiation to generate specialized cells. Stem cell differentiation is tightly regulated by cues from growth factors and chemokines in the extracellular matrix (ECM). HS is present in the ECM and on the surface of cells, where it interacts with signaling molecules and facilitates ligand—receptor interactions that govern cell fate.^{2,3} Thus, HS is a critical regulator of stem cell differentiation.

Received: October 10, 2022 Accepted: March 31, 2023 Published: April 12, 2023





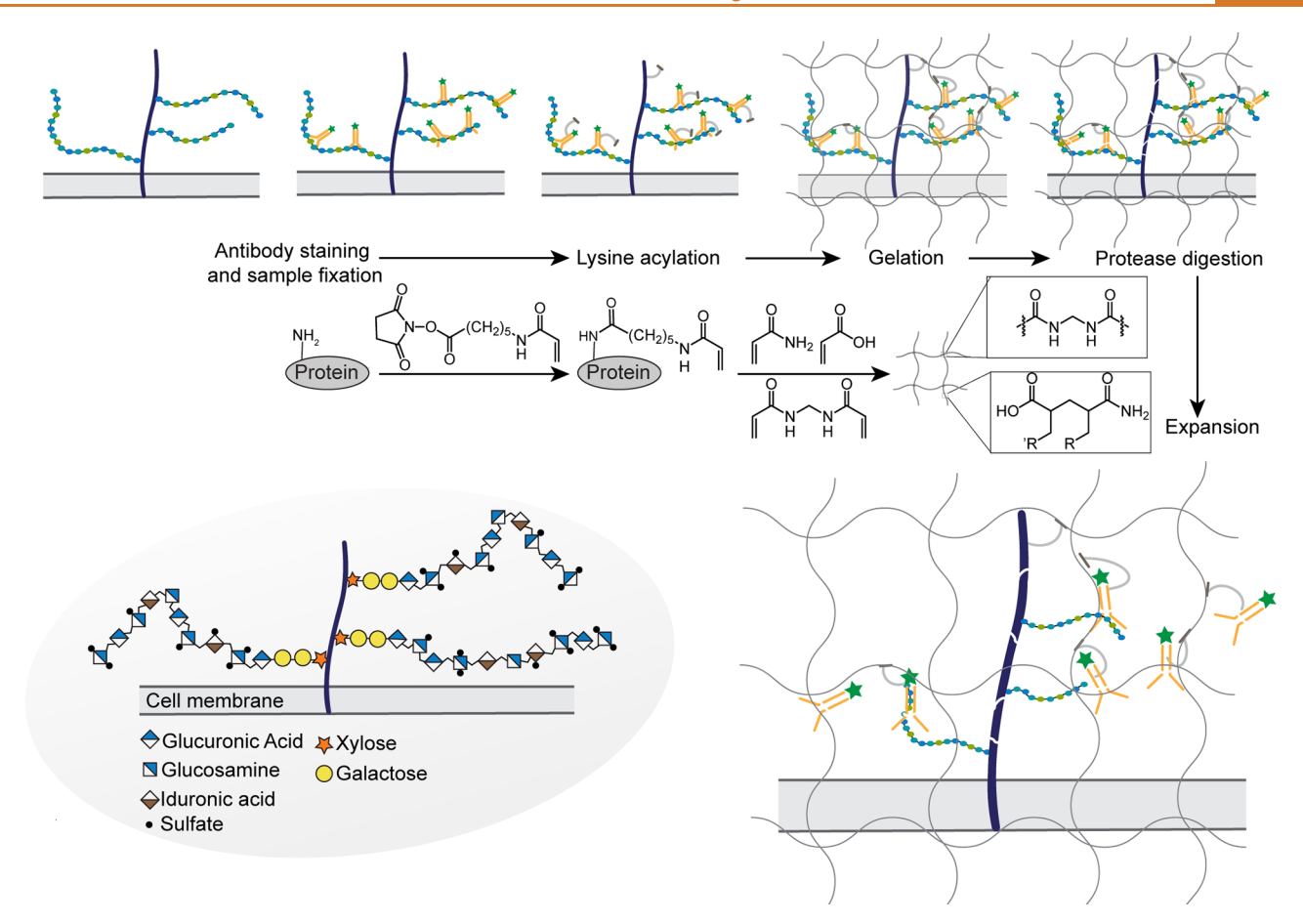


Figure 1. Workflow of protein-retention expansion microscopy (pro-ExM) adapted for visualizing HS.

The HS sulfation pattern is thought to be the primary factor governing its ability to recruit growth factors and participate in signaling. The sulfation pattern changes as cells switch from a proliferative state and undergo lineage differentiation to all three germ layers. These changes arise from HS assembly, which involves an initial biosynthesis of a polymer consisting of a repeating disaccharide unit consisting of *N*-acetyl-D-glucosamine (GlcNAc) and D-glucuronic acid (GlcA). The resulting polysaccharide undergoes multiple enzymatic modifications, including deacetylation, epimerization, and sulfation. Elongated HS chains (40–300 sugar residues, 20–150 nm) can vary in the number and length of the chains, degree and pattern of sulfation, the extent of uronic acid epimerization, and sequence identity. Several methods have been used to relate HS sequence to function.

Analytical methods for examining HS composition and its functional consequences typically require its extraction from cell culture or tissue samples. Liquid chromatography—tandem mass spectrometry (LC—MS/MS) is beginning to identify HS sequences and their associated temporal changes within a sample. Additionally, chemoenzymatically synthesized HS microarrays can reveal insight into how the sulfation pattern influences protein recognition. While changes in sequence can influence protein binding, we postulated that other factors might alter HS function. Specifically, a protein's localization is critical for its activity; therefore, we sought to examine whether HS localization might also influence its function. Many general approaches to characterize HS lose the spatial information related to various cell types and subcellular locations. Assessing HS localization in a cellular context would complement these

approaches. Thus, we set out to visualize changes in cell surface HS as pluripotent stem cells differentiate into distinct lineages.

High-resolution visualization of endogenous glycans could guide our understanding of their structures and functions, ^{17–22} yet glycan imaging has been challenging. The visualization of polysaccharides at the requisite nanometer length scale is underdeveloped. We reasoned that high-resolution imaging could unravel the structural and functional features of polysaccharides like HS. We, therefore, tested the utility of expansion microscopy (ExM), a powerful imaging method in which nanoscale features of a cell are resolved by physically expanding the sample in polyacrylate/acrylamide gel, ^{23–26} for revealing glycan organization. Although it has been widely applied to image biomolecules such as proteins and nucleic acids with nanoscale precision, ²⁷ its potential for glycobiology is largely untapped.

We applied ExM imaging to HS in hPS cells to test whether changes in this polysaccharide could be detected visually throughout the lineage progression. We found that nanostructure of this polysaccharide undergoes striking changes during differentiation. At the proliferative stage, HS of hPS cells appears as hair-like extensions from the cell surface. This extended structure then morphs into discrete puncta during ectoderm but not mesendoderm differentiation. These lineage-specific changes in HS ultrastructure correlate with the cells' ability to bind fibroblast growth factor (FGF). Cells displaying HS as cell surface protrusions showed increased binding to FGF. Differentiated neuronal cells have a highly sulfated variant of HS, but this polysaccharide is distributed within

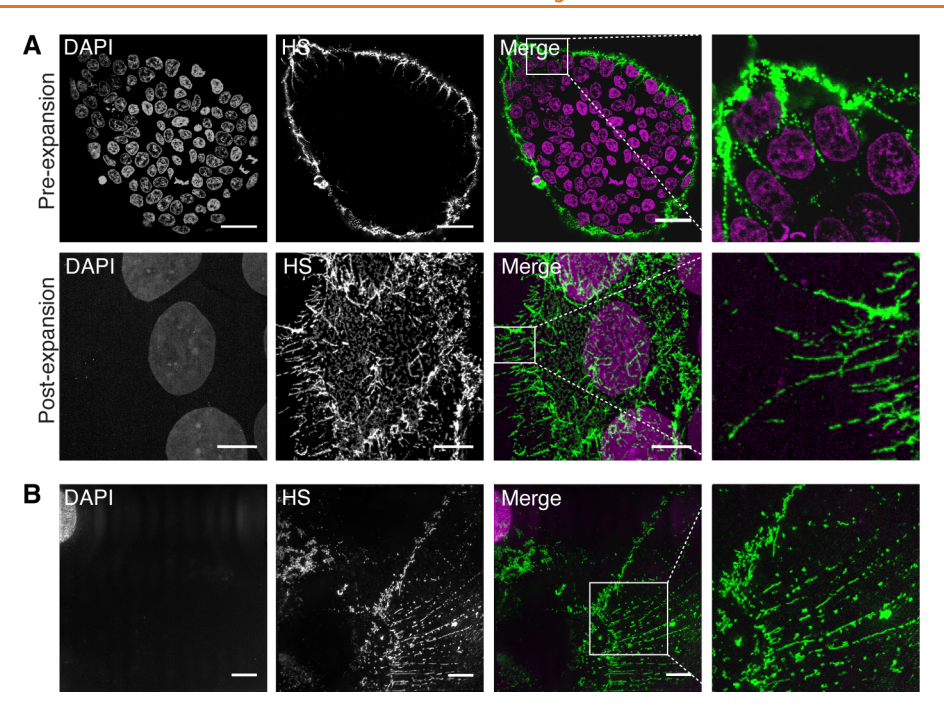


Figure 2. Expansion microscopy enables antibody-mediated visualization of heparan sulfate on the cell surface. (A) Representative Z-stack confocal images of heparan sulfate (HS) in pre-expansion and post-expansion of human pluripotent stem (hPS) cells. HS was labeled using the 10E4 antibody (green), and the nucleus was stained with DAPI (magenta). The scale bar is 30 μ m. (B) Structured illumination microscopy (3D-SIM) images of HS. The scale bar is 5 μ m.

localized puncta on the cell surface. These cells showed decreased binding to FGF. These findings suggest a role for HS nanostructure in modulating signaling in the early stages of human development. Thus, our results highlight how nanoscale imaging of complex glycans can provide insight into how they function. We anticipate that ExM-empowered glycan imaging can identify specific glycan—ligand interactions and dynamic changes in the cellular glycome in development and disease.

RESULTS/DISCUSSION

Using conventional microscopy, we visualized HS in human pluripotent stem (hPS) cells. Undifferentiated hPS cells were exposed to an anti-HS primary antibody (10E4) that binds Nsulfo-D-glucosamine. In HS biosynthesis, the deacetylation and N-sulfation of glucosamine residues is a critical step, and other modification enzymes act subsequently; thus, 10E4 is a general tool for visualizing HS. Immunofluorescence microscopy indicated bright and uniform HS staining on the surface of the cells at the edges of the colonies. These data suggest that the cells at the colony center lacked HS. Still, hPS cell colonies are tightly packed, and we postulated that conventional microscopy might fail to capture the range of cell surface markers, including HS. We therefore employed superresolution imaging using protein-retention expansion microscopy (pro-ExM). We postulated that pro-ExM might provide insight into HS localization beyond that detectable with conventional immunocytochemistry.

A pro-ExM protocol was applied to anchor the formaldehyde-fixed cells to a swellable polyacrylamide gel to expand hPS cells²⁴ (Figure 1). Historically, pro-ExM has been used for protein imaging, and the chemistry used for anchoring components in the gel is not expected to result in direct gelglycan links. Still, HS is appended to proteoglycans, and the protein core provides a means to preserve spatial information.

The fluorescent 10E4 antibody provided a readout for the spatial distribution of the polysaccharide chain.²⁴ Using pro-ExM, we detected a long and elongated hair-like structure displaying HS on the cell surface (Figure 2A, Video S1). These data imply that HS is not restricted to the outer cells of the colony but is present throughout. They also indicate the limitation of low-resolution conventional microscopy as the signal due to HS at the center of a tightly packed colony of hPS cells was not detectable. A pre- and post-expansion nuclear staining comparison indicated that pro-ExM afforded 4-4.5× linear expansion. We examined whether hPS cells have filopodia but found uniform cell membrane morphology, indicating the long HS extensions observed are previously undetected protrusions (Figure S1A). We also verified that the elongated HS structure extends from the base of the actin cytoskeleton (Figure S1B), but the sites of extension have no apparent membrane curvature. A recent publication showed that sterically demanding transmembrane glycoproteins, such as MUC1, can modulate cancer cell membrane shape by inducing membrane protrusions. 28 In contrast, we detected no membrane curvature associated with HS localization.

Few approaches allow for the imaging of glycans in their native environment. Pro evaluate the utility of pro-ExM, we used 3D-structured illumination microscopy (3D-SIM) to test whether the HS nanostructure observed using pro-ExM is consistent with unexpanded images and is not an artifact of distortion during gel formation. We found a similar pattern of HS distribution (Figure 2B) throughout the colony. The spatial distribution and localization of macromolecules underlie their roles as signaling factors. Even the most powerful strategies, such as mass spectrometry imaging, require the release of the glycan where the saccharide ultrastructure and localization are not fully preserved. We found that ExM can be used to pinpoint HS cell surface localization and the detail of the nanostructure in their native environment of hPS cells.

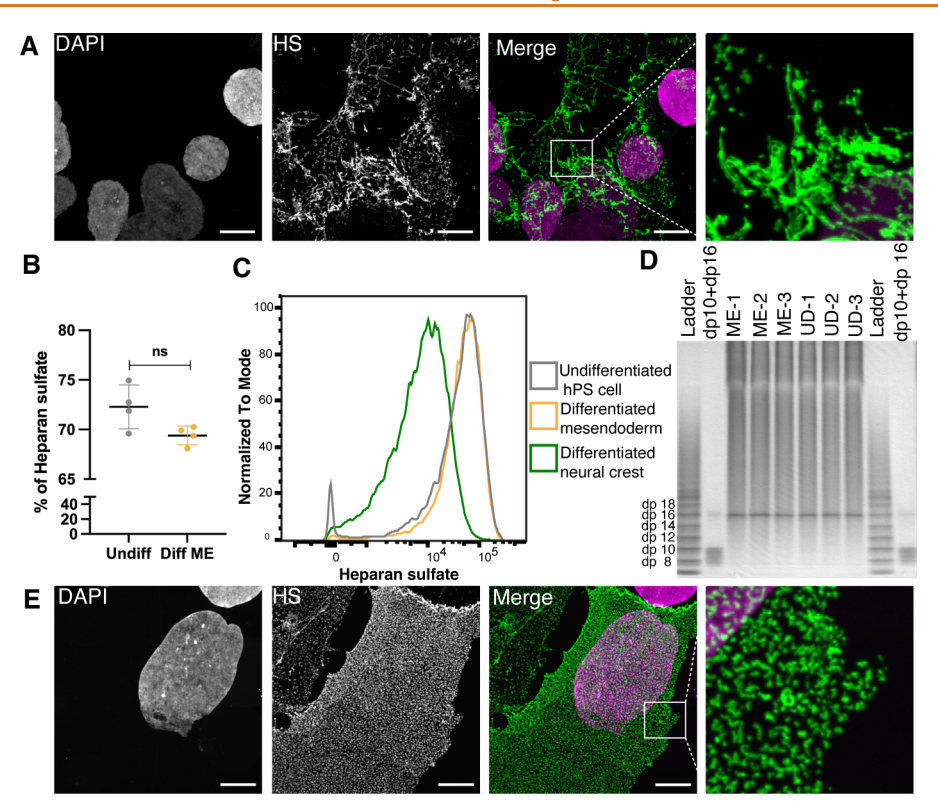


Figure 3. Heparan sulfate content and structure changes in ectodermal cells. (A) Representative confocal Z-stack of pro-ExM image of HS on the surface of the hPS cell-derived mesendoderm cells. (B) LC-MS-based disaccharide analysis was performed to quantify the HS percentage of total isolated GAGs in hPS cells (Undiff) and mesendoderm cells (Diff ME) (n = 4, ns = not significant, unpaired t test). (C) Flow cytometry analysis of surface HS in hPS cells, mesendoderm cells, and neural crest cells using the 10E4 antibody. (D) PAGE analysis of HS from undifferentiated hPS cells (UD, lanes 6-8) and differentiated mesendoderm cells (ME, lanes 3-5) (n = 3). After the PAGE analysis, the gels were visualized with 0.5% (w/v) Alcian blue in a 2% (v/v) aqueous acetic acid solution. The average molecular weights were determined based on heparin oligosaccharides (partially digested) with various degrees of polymerization (dp). (E) Representative confocal Z-stack pro-ExM image of HS puncta on the surface of hPS cell-derived neural crest cells. (A and E) Scale bar, 30 μ m.

These results highlight the advantages of using ExM to visualize cell surface features of hPS cell colonies and underscore that ExM can provide insight into polysaccharides such as HS.

Changes in HS can coincide with cell lineage.³⁰ HS sulfation pattern and chain length can vary across cell types, ^{4,10} and we sought to visualize these changes directly with pro-ExM. We therefore differentiated hPS cells into multipotent mesendoderm cells using a chemically defined protocol.³¹ The imaging data indicate that the HS of mesendoderm cells extends from the cell surface as observed in undifferentiated cells (Figure 3A). To further compare HS in undifferentiated hPS and mesendoderm cells, we used LC-MS to analyze glycosaminoglycans (GAGs) isolated from each cell type.³² The HS mean percentages of the total GAG content in hPS cells and mesendoderm cells were similar, 74% and 69%, respectively (Figure 3B). Flow cytometry data collected using an anti-HS antibody also supported a comparable HS content between the cell types (Figure 3C). We next assessed the molecular weights of HS using polyacrylamide gel electrophoresis (PAGE) to probe whether HS length changes during mesendoderm differentiation (Figure 3D). HS from hPS and mesendoderm cells gave rise to similar band distributions with average molecular weights of 16.2 and 15.8 kDa, respectively. These results suggest that no significant changes occur in HS length and organization during mesendoderm differentiation.

We differentiated hPS cells into neural crest cells,³³ which are ectoderm-derived multipotent migratory cells, to probe HS

changes in the ectoderm. The HS of neural crest cells was distributed in discrete puncta on the cell surface (Figure 3E), demonstrating stark differences between hPS cells and the ectoderm lineage. Because the differentiation yielded a heterogeneous population (Figure S3), we analyzed the neural crest cells using 10E4 and flow cytometry. Consistently, we observed that neural crest cells have lower HS levels than undifferentiated hPS or mesendoderm cells (Figure 3C). To ensure these findings were not biased by the HS sequence, we treated cells with heparinase and then detected with the 3G10 antibody, which recognizes the unsaturated uronic acid generated after heparinase digestion. Consistent with the results with the 10E4 antibody, we observed 3G10 antibody binding to the neural crest cells was decreased relative to hPS cells (Figure S4A). These data highlight the utility of highresolution imaging for capturing the dynamic changes in HS. The dramatic alterations in morphology and distribution of cell surface HS upon differentiation to the ectoderm lineage were accompanied by biochemical changes in growth factor binding (vide infra).

The changes in HS observed as hPS differentiated to neural crest cells led us to examine the distribution of the glycan in terminally differentiated hPS-derived neurons. To this end, we used a dual-SMAD inhibition protocol to convert hPS cells to spinal motor neurons^{34,35} (Figure S5A). In this approach, hPS cells differentiate into neural progenitor (NP) cells by day six and then into spinal motor neuron (hMN) cells by day 13. The application of pro-ExM revealed NP and hMN cells had lower

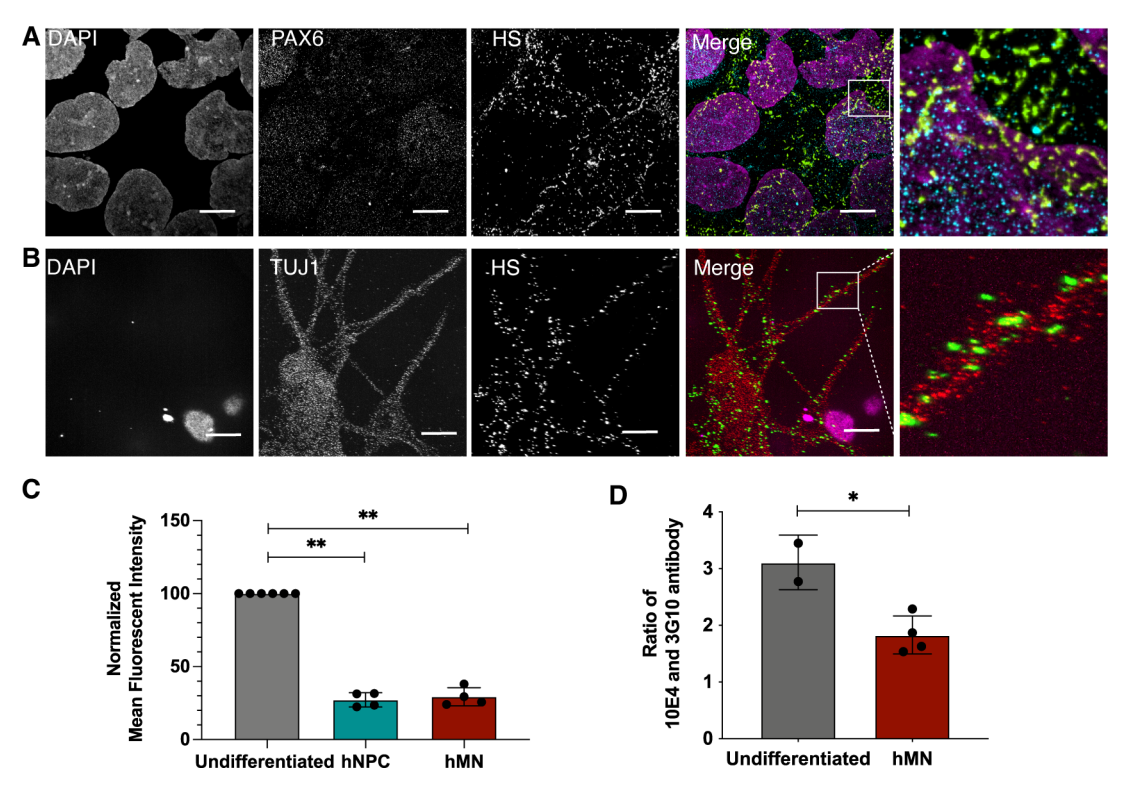


Figure 4. Imaging heparan sulfate in spinal motor neuron differentiation. (A and B) Representative confocal Z-stack of pro-ExM images of HS on the surface of PAX6⁺ NP cells (A) and TUJ1⁺ hMN cells (B). (C) Flow cytometry of cell surface HS of hPS cells, NP cells, and hMN cells (n = 4). Mean fluorescence intensity (MFI; arbitrary units) was calculated using the geometric mean and normalized to that of the undifferentiated hPS cells. (D) hMN cells show a decrease in the ratio of 10E4 antibody to 3G10 antibody binding (n = 4). (A and B) Scale bars, 30 μ m. **p < 0.01, *p < 0.05, unpaired t test in (C and D).

levels of HS than hPS cells (Figure 4A,B). The gradual decrease (Figure S5C) in cell surface HS during neuronal differentiation could be readily detected with the anti-HS antibody (Figure 4C). We observed a diffuse distribution of HS on NP cells, but HS in hMN cells was localized in discrete puncta along the neuronal processes (Figure 4A, B). The punctate HS in hMN cells appeared to be shorter than the HS in the hPS cells.

Analysis of HS length from different cell types using biochemical methods like PAGE requires a homogeneous cell population. Unfortunately, directed differentiation yields heterogeneous cell cultures (Figure S5B) making quantitative, comparative analyses of HS challenging. We used HS-specific antibodies (10E4 and 3G10) to conduct an optical analysis of HS distribution per chain. We therefore used an indirect method. Specifically, we employed the 10E4 antibody as a proxy for total HS and, after the heparinase treatment, the 3G10 antibody as a proxy for HS chain number. Thus, the ratio of 10E4 antibody to 3G10 antibody staining is an on-cell estimate of HS chain length. ³⁶ Although this measurement of HS length has the limitation that 10E4 staining depends on the level of N-sulfation within HS, we reasoned that it would provide some insight into HS length.

We observed that both the 3G10 and the 10E4 antibody signals of hMN cells decreased relative those of hPS cells (Figure 4C and Figure S5D). Moreover, the ratio of 10E4 to 3G10 staining in hMN cells (1.8) was significantly lower than that of hPS cells (3.09), which suggests that there are fewer HS chains in hMNs that are possibly shorter than those of hPS cells (Figure 4D). The ratio of 10E4 to 3G10 staining is also significantly lower in neural crest cells (2.87) than in hPS cells

(4.05) (Figure S4B). Therefore, we postulate that, as the hPS cells differentiate toward ectodermal lineage, the HS chain organization changes from the extended to a punctate structure irrespective of chain length.

Our data suggest that the physical structure of HS changes dramatically in ectoderm lineage-specific multipotent neural crest, neural progenitor cells, or terminally differentiated neurons. By imaging the nanostructure of the glycan during differentiation, we uncovered a lineage-specific morphological change in HS structure. We postulate that these structural changes contribute to the HS function, including its ability to engage specific growth factors and facilitate growth factor signaling.

HS interacts with many growth factors and cytokines at the cell surface. We hypothesized that the changes in HS organization during neuronal differentiation would influence the polysaccharide's interactions with growth factors. We probed the binding of FGF2, an HS-interacting growth factor critical for hPS self-renewal. We compared the cell-surface binding of recombinant FGF2 to hPS, mesendoderm, and hMN cells. When hPS cells and mesendoderm cells were compared, no differences in FGF2 binding were detected, consistent with the similarity of HS in these different cell types (Figure 5A). In contrast, hMN cells' ability to bind FGF2 was reduced. The propensity of hPS cells to bind FGF2 is consistent with studies indicating that FGF signaling is needed to maintain pluripotency. 9,37-39 In the early neural progenitor state, FGF2 promotes the induction of differentiation and survival. Therefore, enhanced FGF2 signaling at the onset of neural differentiation is a prerequisite, whereas inhibiting this signal at subsequent stages promotes the transition into

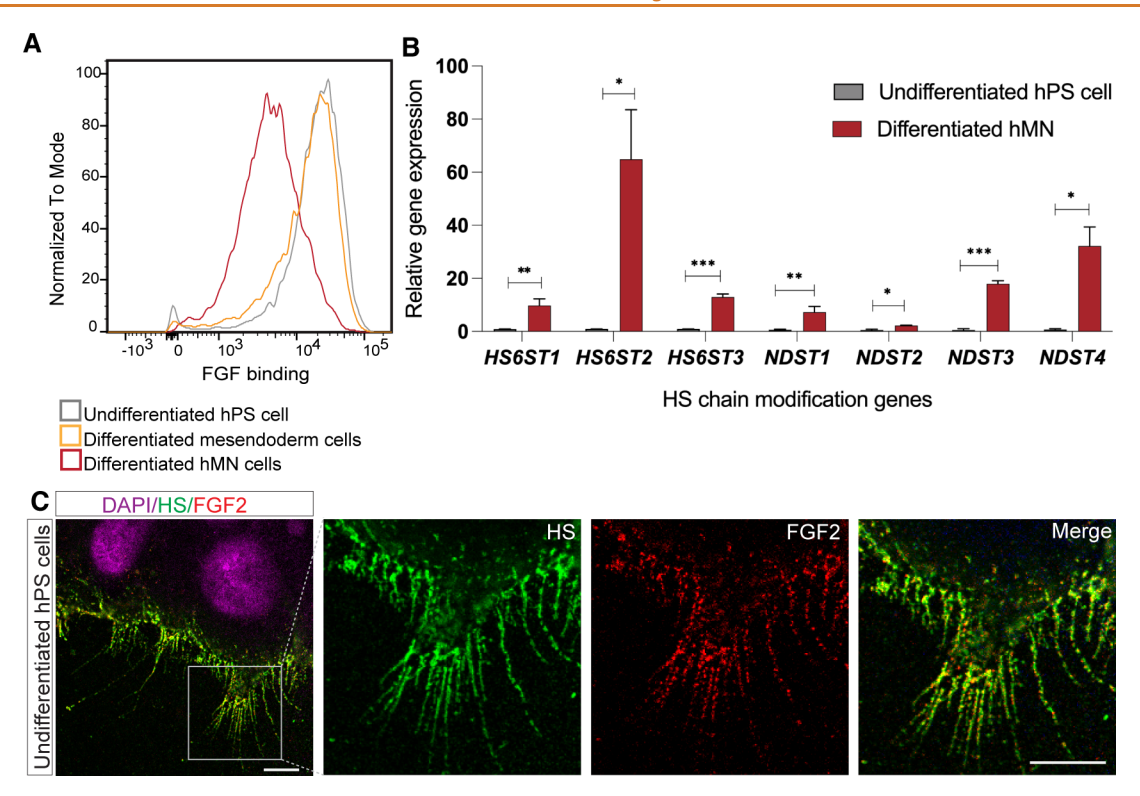


Figure 5. FGF binding to hMN cells and expression of HS modification enzymes. (A) Comparison of the levels of FGF2 bound to HS as hPS cells differentiate toward the neural lineage (hMN). Flow cytometry analysis of FGF2 binding to undifferentiated hPS, hPS-derived mesendoderm, and hMN cells using an anti-FGF2 primary antibody and fluorophore-conjugated secondary antibody. Representative histogram of FGF2 binding assays (N = 3) (B) Quantitative real-time PCR analysis of HS modification enzymes in hPS-derived hMN cells compared to undifferentiated hPS cells (n = 3, biological replicate). An unpaired t test between hPS and hMN cells was used for data analysis. An asterisk denotes a statistically significant difference (***p < 0.001, **p < 0.01, **p < 0.05) between hPS and hMN cells. (C) Representative confocal Z-stack pro-ExM images of FGF2 bound to HS on the surface of undifferentiated hPS cells. DAPI (magenta), HS (green), FGF2 (red). Scale bar, $10 \ \mu m$.

differentiated neurons.^{34,40,41} These findings highlight the complex control of HS—growth factor interactions. In contrast, FGF signaling is a critical regulator of mesendoderm differentiation,⁴² and differentiated mesendoderm and hPS cells display HS with similar ultrastructure. Both cell types also bind readily to FGF2.

The correspondence of gene expression data with the observed signaling differences was not apparent. Specifically, FGF2 binds to sulfated HS, yet the HS biosynthetic genes that lead to HS sulfation are upregulated in hMN cells, including those encoding sulfotransferases (HS6ST1, HS6ST1, HS6ST2, HS6ST3, NDST1, NDST2, NDST3, NDST4) (Figure 5B). The upregulation of the expression of these genes would be predicted to lead to enhanced FGF2 binding. For example, HS sequences with IdoA2S and GlcNS residues have been reported to bind FGF2. 16,43 Additionally, the 6-O-sulfated residues of HS bridge FGF2 and FGFR in mouse embryonic fibroblast models and promote the formation of the ternary complexes that signal. Similarly, in breast cancer cell-line models, 44 2OST1 gene expression facilitates the acquisition of cancer stem cell-like properties by activating FGF signaling pathways. 45 Nevertheless, hMN cells show reduced binding to FGF2.

We postulate that, during ectodermal differentiation, hPS cells reorganize the cell surface HS structure, so the highly sulfated regions are less accessible for the FGF2 binding. We tested this idea further using another ectodermal derivative: differentiated neural crest cells. These cells exhibited higher

binding of 10E4 antibody relative that of the hMN cells. Still, both have punctate HS staining and reduced binding to FGF2 (Figure S6A,B). The details of how HS sequence varies between our different cell types are unknown. Thus, HS sequence variation may influence the affinity of FGF2 for binding or the HS nanostructure. Our data provide strong evidence, however, that the cell surface organization of HS is critical, as this is the attribute that tracks with FGF2 binding.

The changes in HS nanostructure could modulate the binding of various growth factors (e.g., FGF, BMP, $TGF\beta$) during stem cell differentiation. Thus, visualization of HS interactions can uncover changes in its nanostructure and their impact on growth factor interactions. We next tested growth factor binding to the HS chains on the cell surface. ExM enabled high-resolution imaging revealed FGF2 interacting with the HS chains protruding from the hPS cells (Figure 5C). These data suggest that the glycans are readily accessible for growth factor binding. Therefore, ExM for visualizing FGF2 binding on the protruding cell-surface HS chains of undifferentiated cells may further enable the identification of specific location of the glycan chains for specific growth factor binding. Improving the expansion strategy to achieve even higher resolution would be crucial for such an application.

We applied pro-ExM to isolated tissue to determine whether the HS morphologies observed in hPS-derived hMN cells are recapitulated in primary neurons. We imaged brain slices collected from a transgenic mouse producing yellow fluorescent protein (YFP) expressed from a Thy1 promoter.

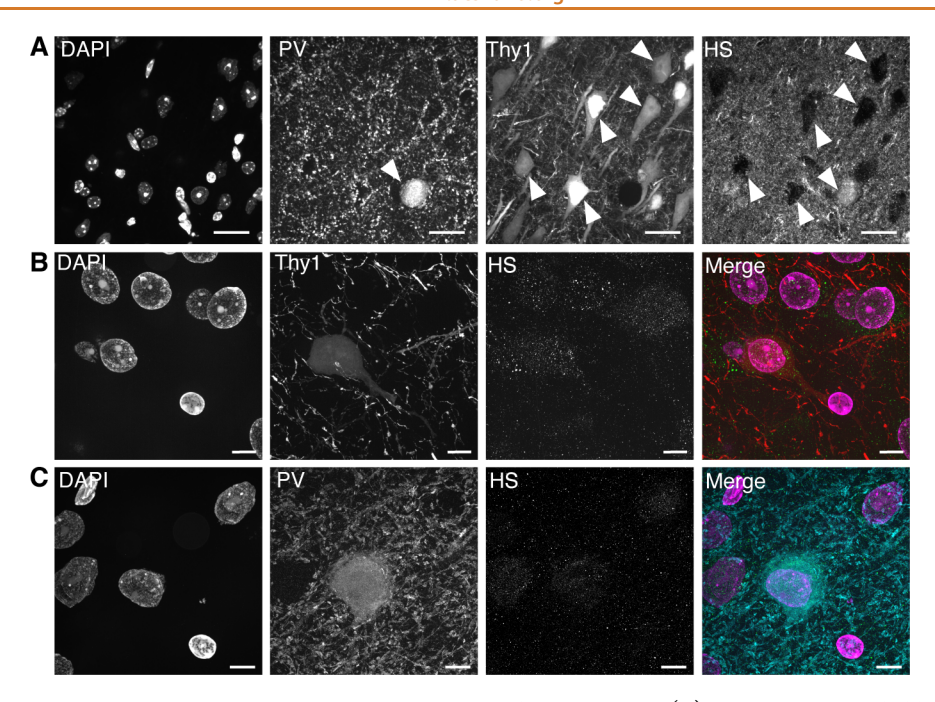


Figure 6. In situ expansion imaging reveals puncta HS in excitatory and inhibitory neurons. (A) Imaging unexpanded brain slice shows HS on PV^+ inhibitory neurons but not in Thy^+ cells. (B and C) Pro-ExM reveals HS puncta both on excitatory (Thy^+) and inhibitory (PV^+) neurons. (A–C) Scale bar, 30 μ m. Images are representative confocal Z-stacks.

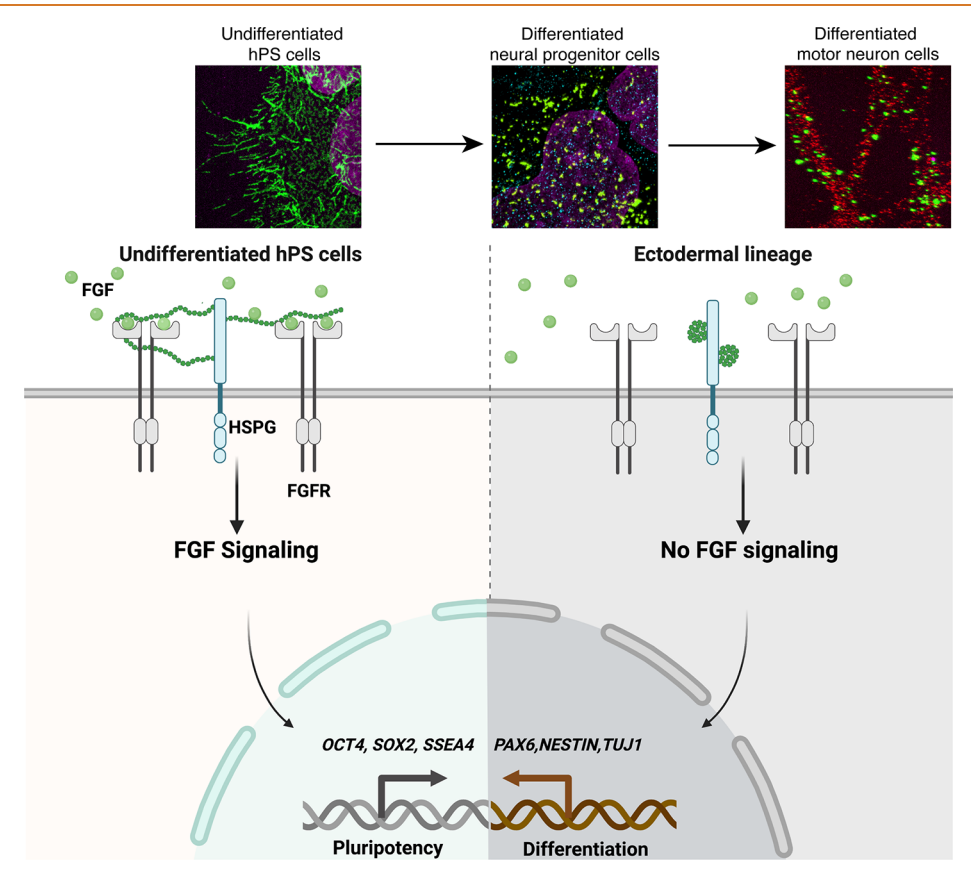


Figure 7. Model for changes in cell surface heparan sulfate proteoglycan ultrastructure that influence cell signaling. ExM images of heparan sulfate (green indicates antibody staining) are overlaid with model of HS-mediated growth factor signaling. In the bottom schematic, heparan sulfate polysaccharides (green) extend from a heparan sulfate proteoglycan (HSPG) and fibroblast growth factor (FGF, light green circle) binds simultaneously to the polysaccharide and the FGF receptor (FGFR) to activate signaling (Image created with Biorender.com).

The YFP identifies the excitatory neurons in the cortex.²⁴ We stained parvalbumin-positive (PV⁺) interneurons for HS to

assess whether the level of this glycan varies between excitatory and inhibitory neurons. In an unexpanded brain slice, we

observed stark differences in HS expression distribution in Thy1⁺ and PV⁺ neurons in the cortex. PV⁺ neurons have significant HS coverage around the cell body, while Thy1⁺ neurons appeared to lack HS (Figure 6A). Still, we posited that these standard conditions might afford low-resolution images in which the HS nanostructure would not be apparent. Indeed, expansion of the brain slices revealed HS puncta in a wide range of cell types, including Thy1+ and PV+ neurons (Figure 6B,C). Thus, pro-ExM afforded a HS signal that was otherwise invisible and confirmed that the HS morphology in neuronal culture resembles that in the mouse cortex.

The morphology shift of HS between pluripotent and neural cells corresponds to a functional change in growth factor interactions. A recent study found that ablation of HS in mouse hippocampal neuron cultures decreases inhibitory synapse density without affecting excitatory synapse density. These findings suggest a significant role for HS in inhibitory synapse development. Our observation of elevated HS expression around interneuron soma supports this conclusion. Our data indicate that further exploration of HS ultrastructure can shed light on HS roles during mammalian neural development and address questions such as how HS expression level is regulated in different cell types and how HS contributes to synapse plasticity in the brain.

CONCLUSIONS

The lack of methods to visualize the ultrastructure of polysaccharides has hindered our understanding of their role in physiological and disease processes. In the case of HS, this has led to a singular focus on how polysaccharide sequence influences binding. Here, using super-resolution imaging by ExM, we found that the glycans' spatial distribution and ultrastructure correlates with growth factor recruitment. Intriguingly, the observation of cell surface protrusions that can present HS to engage growth factors was unexpected but highlights another mechanism by which cells can use glycosaminoglycans to control signaling (Figure 7). Our findings provide an alternative mechanism by which the cell surface polysaccharide HS regulates cell fate.

METHODS/EXPERIMENTAL

Cell culture. H9 (WiCell) human pluripotent stem (hPS) cells were grown with E8 medium (Thermo Fisher Scientific) on tissue culture plates coated with vitronectin (Thermo Fisher Scientific). Cells were maintained at 37 °C in a 5% CO $_2$ incubator. Cells were passaged manually using EDTA (1 mM in PBS, pH 7.4) every 4–5 days, with the addition of 5 μ M ROCK inhibitor (Y-27632 dihydrochloride, Tocris) on the first day to prevent the cell death after dissociation. The cells were routinely tested for mycoplasma contamination (Lookout Mycoplasma PCR Detection Kit, Sigma-Aldrich).

Differentiation of hPS Cells into Different Lineage-Specific Derivatives. The cells were differentiated to mesendoderm using an established protocol. Briefly, the cells were dissociated with EDTA and plated at a density of 100,000 cells per cm² on vitronectin-coated plates with E8 media supplemented with 5 μ M ROCK inhibitor (Y-27632 dihydrochloride, Tocris). The E8 medium was changed every day for the next 2 days. On day three, the media was changed to RPMI-1640 medium (Thermo Fisher Scientific) supplemented with 6 μ M CHIR-99021 (Tocris). Following a 26 h treatment with the differentiation media, the cells were collected for analysis.

Neural crest differentiation was achieved using a chemically defined protocol described previously.³³ In brief, hPS cells were dissociated into single cells using accutase (Thermo Fisher Scientific) and plated at a density of 10,000 cells per cm² on vitronectin-coated plates with

E6 medium supplemented with 5 μ M ROCK inhibitor. The cells were grown for 24 h, and then, the medium was changed into the differentiation medium each of the next 6 days. The differentiation media was prepared by supplementing DMEM-F12 (Life Technologies) with 1× N-2 supplement (Gibco), 1.0 μ M CHIR99021 (Tocris), 2.0 μ M SB431542 (Tocris), 1.0 μ M DMH1 (Tocris), and 15 ng/mL BMP4 (Tocris).

Motor neuron differentiation was achieved using a modified 14-day protocol described previously.³⁵ In brief, hPS cells were dissociated to single cells using accutase and plated at a density of 50,000 cells per cm² on vitronectin-coated culture plates with E8 media supplemented with 5 μ M ROCK inhibitor. As the cells reached >95% confluency, the medium was changed to d0-d5 differentiation media every day for the next 5 days. The d0-d5 differentiation medium was prepared by supplementing the basal medium with 10 μ M SB431542 (Tocris), 100 nM dorsomorphin (Tocris), 1 μ M retinoic acid (Sigma), and 1 μ M smoothened agonist (Tocris). On the day six of differentiation, the medium was changed to d6-d14 differentiation media every day. The d6-d14 medium was prepared by supplementing the basal medium with 5 μ M DAPT (Tocris), 4 μ M SU-5402 (Tocris), 1 μ M retinoic acid (Sigma), and 1 μ M smoothened agonist (Tocris). The basal medium contained a 1:1 mixture of neurobasal media (Life Technologies) and DMEM-F12 (Life Technologies) and was supplemented with 1× B-27 supplement (Gibco), 1× N-2 supplement (Gibco), and 1× Gibco GlutaMAX (Life Technologies).

Immunofluorescence Staining and Imaging. For immunocytochemistry analysis, cells were stained live or after fixation. The cells were rinsed with DMEM/F12 or basal media for live staining, followed by incubation in a blocking buffer (2% BSA in DMEM/F12) for 30 min on ice. The cells were further exposed to anti-HS 10E4 (US Biological, catalog# H1890) at 1:200 in a blocking buffer for 1 h at 4 °C. Then, the cells were exposed to the secondary antibody, IgM-Alexa Fluor 488 (Invitrogen), for 1 h at 4 °C. The stained cells were rinsed twice with cold buffer and fixed with 4% formaldehyde for 10 min at room temperature.

For the staining of internal markers, the fixed samples were permeabilized and blocked with PBS containing 0.1% Triton X-100 and 2% bovine serum albumin (BSA). All primary antibodies were incubated in a blocking buffer overnight at 4 °C or 1 h at room temperature. The primary antibodies and dilutions used are described in Table S1. The secondary antibody staining was performed with Alexa Fluor 488, 594, 647, or Atto 647N conjugated antimouse, rabbit, chicken, or goat IgG antibodies (Invitrogen) diluted at 1:1000 in the blocking buffer and exposed to cells for 1 h at room temperature. For the samples for expansion, the secondary antibodies were used at 1:200 dilution. The cell nuclei were counterstained with DAPI dilactate (1:10000, Molecular Probes). Images were collected with a Nikon A1R ultra-fast spectral scanning confocal microscope. The 3D-SIM super resolution images were collected using an applied precision DeltaVision-OMX super-resolution microscope. Images were analyzed using Fiji.

Pro-ExM of Stem Cell Culture. The following steps were performed as described previously. ^{24–26,47} Immunostained and fixed culture was incubated in 0.1 mg/mL Acryloyl-X, SE (Thermo Fisher Scientific) in PBS at 4 °C overnight. The cell culture was then washed twice with PBS for 15 min. Monomer solution (1× PBS, 2 M NaCl, 8.625% (w/w) sodium acrylate, 2.5% (w/w) acrylamide, 0.15% (w/w) N,N'-methylenebis(acrylamide)), ammonium persulfate (APS) (10% w/w in water), and tetramethylethylenediamine (TEMED) (10% w/w in water) were stored frozen in aliquots. Upon thawing, monomer solution, water, TEMED solution, and APS solution were mixed in a ratio of 47:1:1:1 and kept on ice. The solution mixture was added to the cell culture and covered with a parafilm-wrapped coverslip. The gelation chamber was then put under nitrogen and moved to a humidified 37 °C incubator for 1 h.

Gel was further incubated with Proteinase K at 8 units/mL (New England Biolabs) in digestion buffer (50 mM Tris pH 8.0, 1 mM EDTA, 0.5% Triton X-100, 1 M NaCl) at room temperature for overnight. Digested gels were placed in large volumes of deionized

water to expand. Water was replaced every 30 min until the gel no longer expanded.

Brain Tissue Preparation. All procedures involving Thy1-YFP-H transgenic mice (Jackson Laboratory) followed the US National Institute of Health Guide for the Care and Use of Laboratory Animals and were approved by the Massachusetts Institute of Technology Committee on Animal Care. Animals were housed in groups in standardized cages (temperature, $20-22\,^{\circ}\mathrm{C}$; humidity 30-70%) with a 12 h light/12 h dark cycle with unrestricted access to food and water. Mice 2-4 months old were deeply anesthetized using isoflurane in room air. Mice were transcardially perfused at room temperature with ice-cold 10 mL of 4% paraformaldehyde in phosphate-buffered saline. Fixed brains were sectioned to 50 μ m thick slices with a vibrating microtome (Leica VT1000S) and stored in PBS at 4 $^{\circ}\mathrm{C}$.

Immunostaining of Unexpanded Tissue. Fixed brain slices were incubated in MAXblock Blocking Medium (Active Motif #15252) at 4 °C for overnight, followed by incubating with primary antibody (1:200) in MAXbind staining medium (Active Motif #15253) at 4 °C overnight. The slices were then washed with MAXwash washing medium (Active Motif #15254) four times for 30 min each at room temperature. The slices were incubated with secondary antibody (1:200) in MAXbind staining medium, followed by four washes for 30 min with MAXwash washing buffer at room temperature.

Anchoring, Gelation, Digestion, and Expansion of Intact Tissue. The following steps were performed as described previously. ^{24–26,47} Fixed and immunostained slices were incubated in 0.1 mg/mL Acryloyl-X, SE in PBS at 4 °C overnight. Monomer solution (1× PBS, 2 M NaCl, 8.625% (w/w) sodium acrylate, 2.5% (w/w) acrylamide, 0.15% (w/w) N,N'-methylenebis(acrylamide)), ammonium persulfate (APS) (10% w/w in water), tetramethylethylenediamine (TEMED) (10% w/w in water), and 4-hydroxy-2,2,6,6-tetramethylpiperidin-1-oxyl (4-HT-TEMPO) inhibitor (0.5% w/w in water) were stored frozen in aliquots. Upon thawing, monomer solution, 4-HT-TEMPO solution, TEMED solution, and APS solution were mixed in a ratio of 47:1:1:1 and kept on ice. Tissue slices were incubated in the solution mixture for 30 min on ice and transferred to a humidified 37 °C incubator under nitrogen for 2 h.

The gel was then incubated with Proteinase K 8 units/mL (New England Biolabs) in digestion buffer (50 mM Tris pH 8, 1 mM EDTA, 0.5% Triton X-100, 1 M NaCl) at 37 °C overnight. Digested gels were placed in large volumes of deionized water to expand. Water was replaced every 30 min until the gel no longer expanded.

Detection of HS by Flow Cytometry. Undifferentiated hPS cells and the differentiated cells derived from hPS cells were analyzed by flow cytometry according to Holley et al. 48 with slight modifications. Briefly, cells were dissociated using warm accutase and resuspended in cold DMEM/F12 supplemented with 5 μ M ROCK inhibitor. Cells were washed twice with cold PBS followed by incubation with 500 μ L of Ghost Dye Violet 450 cell stain (1:1000, Tonbo Biosciences) on ice for 30 min. Cells were then rinsed with cold buffer (PBS, pH 7.4 supplemented with 0.1% BSA). Cells were further incubated with anti-HS 10E4 at 1:200 dilution for 1 h, at 4 °C and then with the secondary antibody, IgM-PE (Santa Cruz) (1.5 μ L/test), for 1 h, at 4 °C, followed by fixation with 1% formaldehyde in cold PBS. Data were collected using the Attune NxT Flow Cytometer (Thermo Fisher Scientific) and analyzed using FlowJo software. The percentage of positive cells was established by comparing wild-type cells to HS knockout cells.

Distribution of HS per Chain Detected by Flow Cytometry. Undifferentiated hPS cells and hPS-derived hMN cells were treated with a cocktail of heparinase enzymes composed of *Bacteroides* heparinase I (New England Biolabs, #P0735), heparinase II (New England Biolabs, #P0736), and heparinase III (New England Biolabs, #P0737). Each enzyme was used at 4 unit/mL concentration in the cocktail. Cells were incubated for 2–2.5 h at the 37 °C in a 5% CO₂ incubator. After the heparinases treatment, cells were dissociated using warm accutase and rinsed with cold PBS followed by incubation with 500 μ L of Ghost Dye Violet 450 cell stain on ice for 30 min.

Cells were then rinsed with cold buffer (PBS, pH 7.4 supplemented with 0.1% BSA). Cells were further exposed to anti-HS 10E4 at 1:200 or anti-HS 3G10 (Amsbio # 370260-S) for 1 h, at 4 °C. After two rinses with cold buffer, cells were incubated with IgM-PE (Santa Cruz) or IgM-Alexa Fluor 488 (Invitrogen) for 1 h, at 4 °C. The stained cells were rinsed twice with cold buffer and fixed with 1% formaldehyde in cold PBS. Data were collected using an Attune NxT flow cytometer and analyzed using FlowJo software. HS knockout hPS cells were used as a negative control.

FGF2 Cell Surface Binding Detected by Flow Cytometry. H9 hPS cells and differentiated derivatives were dissociated using warm accutase and rinsed three times with cold buffer (DMEM/F12 containing 1% BSA and 5 μ M Y-27632) to remove excess growth factors from the media. The cells were then incubated with 1 μ g/mL FGF2 (Waisman Biomanufacturing) and Ghost Dye Violet 450 cell stain (1:1000) in ice for 30 min. Cells were then rinsed with cold buffer (PBS, pH 7.4 supplemented with 0.1% BSA). Bound FGF2 was detected by anti-FGF2 (1:100, LifeSpan Biosciences) labeled with a secondary antibody (mouse IgG_{2a+b} , BD Biosciences). Data were collected using an Attune NxT flow cytometer (Thermo Fisher Scientific) and analyzed using FlowJo software.

GAG Preparation and Disaccharide Analysis. Cells were proteolyzed at 55 °C with 300 µL of 20 mg/mL actinase E for 24 h and followed by actinase E deactivation at 100 °C for 30 min. The amount of the above solution containing one million cells was transferred to a 3 kDa molecular weight cutoff (MWCO) spin tube. The filter unit was washed three times with 400 μ L of distilled water and then added to 300 μL of digestion buffer (50 mM ammonium acetate containing 2 mM calcium chloride adjusted to pH 7.0). Recombinant heparin lyase I, II, and III (pH optima 7.0-7.5) and recombinant chondroitin lyase ABC (pH optimum 7.4, 10 mU each) were added to each filter unit containing sample and incubated at 37 °C for 24 h. The enzymatic digestion was terminated by ultrafiltration through the 3 kDa spin tube. The filtrate was collected, and the filter unit was washed twice with 200 μL of distilled water. All the filtrates containing the disaccharide products were combined and dried via freeze-drying. The dried samples were AMAC-labeled by adding 10 μ L of 0.1 M AMAC in DMSO/acetic acid (17/3, V/V), incubating at rt for 10 min, and, then, added with 10 μ L of 1 M aqueous sodium cyanoborohydride and incubating for 1 h at 45 °C. A mixture containing all 17 disaccharide standards prepared at 0.5 $ng/\mu L$ was similarly AMAC-labeled and used as an external standard for each run. After the AMAC-labeling reaction, the samples were centrifuged, and each supernatant was recovered.

LC was performed on an Agilent 1200 LC system at 45 °C using an Agilent Poroshell 120 ECC18 (2.7 μm , 3.0 mm \times 50 mm) column. Mobile phase A (MPA) was a 50 mM aqueous ammonium acetate solution, and mobile phase B (MPB) was methanol. The mobile phase passed through the column at a flow rate of 300 $\mu L/min$. The gradient was 0–10 min, 5–45% B; 10–10.2 min, 45–100% B; 10.2–14 min, 100% B; 14–22 min, 100–5% B. Injection volume is 5 μL .

A triple quadrupole mass spectrometry system equipped with an ESI source (Thermo Fisher Scientific) was used as a detector. The online MS analysis was at the Multiple Reaction Monitoring (MRM) mode. MS parameters: negative ionization mode with a spray voltage of 3000 V, a vaporizer temperature of 300 $^{\circ}$ C, and a capillary temperature of 270 $^{\circ}$ C.

Polyacrylamide Gel Electrophoresis (PAGE). The proteolyzed cell solution containing 10–16 million cells was subjected to chondroitin lyase ABC digestion. The chondroitin sulfate disaccharides were removed by ultrafiltration through a 3 kDa molecular weight cutoff (MWCO) spin tube. The filter unit was washed twice with 200 μ L of distilled water. The HS GAG that remained in the filter was collected and lyophilized. The lyophilized samples were then dissolved in 400 μ L of a solution of denaturing buffer (8 M urea containing 2% wt. CHAPS), bound to Vivapure Q Mini H spin column, washed twice with 400 μ L of denaturing buffer, and washed three times with 400 μ L of 0.2 M sodium chloride solution. The HS GAG components were then eluted from the spin column with three 400 μ L volumes of 16% aqueous sodium chloride solution and

collected by ultrafiltration through a 3 kDa molecular weight cutoff spin tube. The filter unit was washed twice with 400 μ L of distilled water to remove salt, and the HS GAG in the filter was collected and freeze-dried. The lyophilized samples were dissolved in 30 μ L of loading buffer for PAGE. Three microliters of the above solution was loaded in native PAGE using 0.75 mm × 6.8 cm × 8.6 cm mini gels cast from 15% resolving gel monomer solution and 5% stacking gel monomer solution. Heparin partially digested was used as molecular markers (ladder). The mini gels were subjected to electrophoresis at a constant 190 V for 30 min and visualized with 0.5% (w/v) Alcian blue in a 2% (v/v) aqueous acetic acid solution. Molecular weight analysis was performed with UNSCANIT software (Silk Scientific) using the logarithmic relationship between the GAG molecular weight and its migration distance.

RNA Preparation and qRT-PCR. Total RNA was extracted from undifferentiated hPS and d13 hMN using TRIzol (Life Technologies) and a direct-zol RNA MiniPrep kit (Zymo Research) per manufacturer instructions. RNA (1 μ g) from each sample was reverse transcribed to cDNA using an iScript cDNA Synthesis Kit (Bio-Rad). The qPCR was performed on the CFX Connect (Bio-Rad) using iTaq Universal SYBR Green Supermix (Bio-Rad) and gene-specific primers. GAPDH was used as a reference gene for normalization. The primer sequences used are described in Table S2. The relative gene expression levels were determined using the δ - δ CT (ddCt) method, and the error bars were determined from the standard deviation of at least three biological replicates.

ASSOCIATED CONTENT

3 Supporting Information

The Supporting Information is available free of charge at https://pubs.acs.org/doi/10.1021/acsnano.2c10072.

Video of heparan sulfate on the surface of undifferentiated hPS cells (post-expansion) (MP4)

Video of heparan sulfate on the surface of hPS cellsderived motor neurons (post-expansion) (MP4)

Figures of visualization of heparan sulfate on the cell surface of hPS with or without heparinase treatment, flow cytometry gating strategy for neural crest cells and differentiated motor neuron cells, change in heparan sulfate as hPS differentiated to neural crest cells and hMN cells, differential FGF binding to NC cells, and visualization of FGF binding to NC cells and tables of primary antibodies and qPCR primer sequences used (PDF)

AUTHOR INFORMATION

Corresponding Author

Laura L. Kiessling — Department of Chemistry, Massachusetts Institute of Technology, Cambridge, Massachusetts 02139, United States; The Broad Institute of MIT and Harvard, Cambridge, Massachusetts 02142, United States; Koch Institute, MIT, Cambridge, Massachusetts 02139, United States; orcid.org/0000-0001-6829-1500; Phone: +1(617)258-6008; Email: kiesslin@mit.edu

Authors

Deena Al Mahbuba — Department of Chemistry, Massachusetts Institute of Technology, Cambridge, Massachusetts 02139, United States; Occid.org/0000-0003-1951-6165

Sayaka Masuko — Department of Chemistry, Massachusetts Institute of Technology, Cambridge, Massachusetts 02139, United States; oorcid.org/0000-0002-9072-0356

Shiwei Wang – Department of Chemistry, Massachusetts Institute of Technology, Cambridge, Massachusetts 02139,

- United States; McGovern Institute for Brain Research, MIT, Cambridge, Massachusetts 02139, United States
- Deepsing Syangtan Department of Chemistry, Massachusetts Institute of Technology, Cambridge, Massachusetts 02139, United States
- Jeong Seuk Kang John A. Paulson School of Engineering and Applied Sciences, Harvard University, Cambridge, Massachusetts 02139, United States
- Yuefan Song Department of Chemistry and Chemical Biology, Center for Biotechnology and Interdisciplinary Studies, Rensselaer Polytechnic Institute, Troy, New York 12180, United States
- Tay Won Shin − Media Arts and Sciences, MIT, Cambridge, Massachusetts 02139, United States; orcid.org/0000-0002-0061-522X
- Ke Xia Department of Chemistry and Chemical Biology, Center for Biotechnology and Interdisciplinary Studies, Rensselaer Polytechnic Institute, Troy, New York 12180, United States
- Fuming Zhang Department of Chemistry and Chemical Biology, Center for Biotechnology and Interdisciplinary Studies, Rensselaer Polytechnic Institute, Troy, New York 12180, United States; © orcid.org/0000-0003-2803-3704
- Robert J. Linhardt Department of Chemistry and Chemical Biology, Center for Biotechnology and Interdisciplinary Studies, Rensselaer Polytechnic Institute, Troy, New York 12180, United States; orcid.org/0000-0003-2219-5833
- Edward S. Boyden McGovern Institute for Brain Research, Department of Brain and Cognitive Sciences, Media Arts and Sciences, Department of Biological Engineering, Koch Institute, and Centers for Neurobiological Engineering and Extreme Bionics, MIT, Cambridge, Massachusetts 02139, United States; Howard Hughes Medical Institute, Cambridge, Massachusetts 02139, United States

Complete contact information is available at: https://pubs.acs.org/10.1021/acsnano.2c10072

Author Contributions

Conceptualization: D.A.M., S.M., and L.L.K. Methodology: D.A.M., S.M., S.W., D.S., J.S.K, Y.S., R.J.L., E.S.B., and L.L.K. Investigation: D.A.M., S.M., S.W., D.S., J.S.K., Y.S., T.W.S., K.X., and F.Z. Supervision: R.J.L., E.S.B., and L.L.K. Writing—original draft: D.A.M. and L.L.K. Writing—review and editing: all authors.

Notes

The authors declare the following competing financial interest(s): E.S.B. is a co-inventor on multiple patents and patent applications related to expansion microscopy and a co-founder of a company seeking commercial applications of expansion microscopy. The other authors declare that they have no competing interests.

ACKNOWLEDGMENTS

The research reported in this publication was supported by the National Institute of Health grants R01GM49975 and U01GM125288 (L.L.K.), R01AI055258 (L.L.K.), R01EB024261 (E.S.B.), DK11958 (R.J.L.), AI156573 (R.J.L.), and GlycoMIP, a NSF Materials Innovation Platform funded through Cooperative Agreement DMR-1933525 (R.J.L.). The authors also acknowledge an NSF Graduate Research Fellowship grant 1122374 (to T.W.S.). L.L.K. and E.S.B. acknowledge Open Philanthropy and Good Ventures for

funding. The authors thank J. Kuhn, from the microscopy facility of Koch institute for integrative cancer research at MIT for the support in super-resolution imaging. D.A.M. thanks A. Dugan, V. Marando, and C. Zhang of Massachusetts Institute of Technology for the thoughtful discussions. E.S.B. acknowledges L. Yang, J. Doerr, and K. Octavio.

REFERENCES

- (1) Turnbull, J.; Powell, A.; Guimond, S. Heparan Sulfate: Decoding a Dynamic Multifunctional Cell Regulator. *Trends Cell Biol.* **2001**, *11*, 75–82.
- (2) Bulow, H. E.; Hobert, O. The Molecular Diversity of Glycosaminoglycans Shapes Animal Development. *Annu. Rev. Cell Dev Biol.* **2006**, 22, 375–407.
- (3) Esko, J. D.; Selleck, S. B. Order out of Chaos: Assembly of Ligand Binding Sites in Heparan Sulfate. *Annu. Rev. Biochem.* **2002**, 71, 435–471.
- (4) Nairn, A. V.; Kinoshita-Toyoda, A.; Toyoda, H.; Xie, J.; Harris, K.; Dalton, S.; Kulik, M.; Pierce, J. M.; Toida, T.; Moremen, K. W.; Linhardt, R. J. Glycomics of Proteoglycan Biosynthesis in Murine Embryonic Stem Cell Differentiation. *J. Proteome Res.* **2007**, *6*, 4374–4387.
- (5) Johnson, C. E.; Crawford, B. E.; Stavridis, M.; Ten Dam, G.; Wat, A. L.; Rushton, G.; Ward, C. M.; Wilson, V.; van Kuppevelt, T. H.; Esko, J. D.; Smith, A.; Gallagher, J. T.; Merry, C. L. Essential Alterations of Heparan Sulfate During the Differentiation of Embryonic Stem Cells to Sox1-Enhanced Green Fluorescent Protein-Expressing Neural Progenitor Cells. Stem Cells 2007, 25, 1913–1923.
- (6) Smith, R. A.; Meade, K.; Pickford, C. E.; Holley, R. J.; Merry, C. L. Glycosaminoglycans as Regulators of Stem Cell Differentiation. *Biochem. Soc. Trans.* **2011**, *39*, 383–387.
- (7) Baldwin, R. J.; ten Dam, G. B.; van Kuppevelt, T. H.; Lacaud, G.; Gallagher, J. T.; Kouskoff, V.; Merry, C. L. A Developmentally Regulated Heparan Sulfate Epitope Defines a Subpopulation with Increased Blood Potential During Mesodermal Differentiation. *Stem Cells* **2008**, *26*, 3108–3118.
- (8) Dam, G. B.; Kurup, S.; van de Westerlo, E. M.; Versteeg, E. M.; Lindahl, U.; Spillmann, D.; van Kuppevelt, T. H. 3-O-Sulfated Oligosaccharide Structures Are Recognized by Anti-Heparan Sulfate Antibody Hs4c3. *J. Biol. Chem.* **2006**, *281*, 4654–4662.
- (9) Sarrazin, S.; Lamanna, W. C.; Esko, J. D. Heparan Sulfate Proteoglycans. *Cold Spring Harb Perspect Biol.* **2011**, 3, a004952.
- (10) Kreuger, J.; Kjellen, L. Heparan Sulfate Biosynthesis: Regulation and Variability. J. Histochem Cytochem 2012, 60, 898–907.
- (11) Zaia, J. Glycosaminoglycan Glycomics Using Mass Spectrometry. *Mol. Cell Proteomics* **2013**, *12*, 885–892.
- (12) Turnbull, J. E.; Hopwood, J. J.; Gallagher, J. T. A Strategy for Rapid Sequencing of Heparan Sulfate and Heparin Saccharides. *Proc. Natl. Acad. Sci. U. S. A.* **1999**, *96*, 2698–2703.
- (13) Venkataraman, G.; Shriver, Z.; Raman, R.; Sasisekharan, R. Sequencing Complex Polysaccharides. *Science* **1999**, 286, 537–542.
- (14) Kreuger, J.; Salmivirta, M.; Sturiale, L.; Gimenez-Gallego, G.; Lindahl, U. Sequence Analysis of Heparan Sulfate Epitopes with Graded Affinities for Fibroblast Growth Factors 1 and 2. *J. Biol. Chem.* **2001**, *276*, 30744–30752.
- (15) Yang, B.; Solakyildirim, K.; Chang, Y.; Linhardt, R. J. Hyphenated Techniques for the Analysis of Heparin and Heparan Sulfate. *Anal Bioanal Chem.* **2011**, 399, 541–557.
- (16) Horton, M.; Su, G.; Yi, L.; Wang, Z.; Xu, Y.; Pagadala, V.; Zhang, F.; Zaharoff, D. A.; Pearce, K.; Linhardt, R. J.; Liu, J. Construction of Heparan Sulfate Microarray for Investigating the Binding of Specific Saccharide Sequences to Proteins. *Glycobiology* **2021**, *31*, 188–199.
- (17) Tian, E.; Hagen, K. G. T. O-Linked Glycan Expression During Drosophila Development. *Glycobiology* **2007**, *17*, 820–827.

- (18) Truong, L. D.; Phung, V. T.; Yoshikawa, Y.; Mattioli, C. A. Glycoconjugates in Normal Human Kidney. A Histochemical Study Using 13 Biotinylated Lectins. *Histochemistry* **1988**, *90*, 51–60.
- (19) Prescher, J. A.; Bertozzi, C. R. Chemistry in Living Systems. *Nat. Chem. Biol.* **2005**, *1*, 13–21.
- (20) Marando, V. M.; Kim, D. E.; Calabretta, P. J.; Kraft, M. B.; Bryson, B. D.; Kiessling, L. L. Biosynthetic Glycan Labeling. *J. Am. Chem. Soc.* **2021**, *143*, 16337.
- (21) Hsu, T. L.; Hanson, S. R.; Kishikawa, K.; Wang, S. K.; Sawa, M.; Wong, C. H. Alkynyl Sugar Analogs for the Labeling and Visualization of Glycoconjugates in Cells. *Proc. Natl. Acad. Sci. U. S. A.* **2007**, *104*, 2614–2619.
- (22) Paessens, L. C.; Garcia-Vallejo, J. J.; Fernandes, R. J.; van Kooyk, Y. The Glycosylation of Thymic Microenvironments. A Microscopic Study Using Plant Lectins. *Immunol. Lett.* **2007**, *110*, 65–73.
- (23) Gallagher, B. R.; Zhao, Y. Expansion Microscopy: A Powerful Nanoscale Imaging Tool for Neuroscientists. *Neurobiol. Dis.* **2021**, *154*, 105362.
- (24) Tillberg, P. W.; Chen, F.; Piatkevich, K. D.; Zhao, Y.; Yu, C. C.; English, B. P.; Gao, L.; Martorell, A.; Suk, H. J.; Yoshida, F.; DeGennaro, E. M.; Roossien, D. H.; Gong, G.; Seneviratne, U.; Tannenbaum, S. R.; Desimone, R.; Cai, D.; Boyden, E. S. Protein-Retention Expansion Microscopy of Cells and Tissues Labeled Using Standard Fluorescent Proteins and Antibodies. *Nat. Biotechnol.* **2016**, 34, 987–992.
- (25) Chen, F.; Tillberg, P. W.; Boyden, E. S. Optical Imaging. Expansion Microscopy. *Science* **2015**, *347*, 543–548.
- (26) Wassie, A. T.; Zhao, Y.; Boyden, E. S. Expansion Microscopy: Principles and Uses in Biological Research. *Nat. Methods* **2019**, *16*, 33–41.
- (27) Sun, D. E.; Fan, X.; Shi, Y.; Zhang, H.; Huang, Z.; Cheng, B.; Tang, Q.; Li, W.; Zhu, Y.; Bai, J.; Liu, W.; Li, Y.; Wang, X.; Lei, X.; Chen, X. Click-Exm Enables Expansion Microscopy for All Biomolecules. *Nat. Methods* **2021**, *18*, 107–113.
- (28) Lu, C. H.; Pedram, K.; Tsai, C. T.; Jones, T. t.; Li, X.; Nakamoto, M. L.; Bertozzi, C. R.; Cui, B. Membrane Curvature Regulates the Spatial Distribution of Bulky Glycoproteins. *Nat. Commun.* **2022**, *13*, 3093.
- (29) Powers, T. W.; Neely, B. A.; Shao, Y.; Tang, H.; Troyer, D. A.; Mehta, A. S.; Haab, B. B.; Drake, R. R. Maldi Imaging Mass Spectrometry Profiling of N-Glycans in Formalin-Fixed Paraffin Embedded Clinical Tissue Blocks and Tissue Microarrays. *PLoS One* **2014**, *9*, e106255.
- (30) Gasimli, L.; Hickey, A. M.; Yang, B.; Li, G.; dela Rosa, M.; Nairn, A. V.; Kulik, M. J.; Dordick, J. S.; Moremen, K. W.; Dalton, S.; Linhardt, R. J. Changes in Glycosaminoglycan Structure on Differentiation of Human Embryonic Stem Cells Towards Mesoderm and Endoderm Lineages. *Biochim. Biophys. Acta* **2014**, *1840*, 1993—2003.
- (31) Lian, X.; Bao, X.; Zilberter, M.; Westman, M.; Fisahn, A.; Hsiao, C.; Hazeltine, L. B.; Dunn, K. K.; Kamp, T. J.; Palecek, S. P. Chemically Defined, Albumin-Free Human Cardiomyocyte Generation. *Nat. Methods* **2015**, *12*, 595–596.
- (32) Volpi, N.; Galeotti, F.; Yang, B.; Linhardt, R. J. Analysis of Glycosaminoglycan-Derived, Precolumn, 2-Aminoacridone-Labeled Disaccharides with Lc-Fluorescence and Lc-Ms Detection. *Nat. Protoc* **2014**, *9*, 541–558.
- (33) Hackland, J. O. S.; Frith, T. J. R.; Andrews, P. W. Fully Defined and Xeno-Free Induction of Hpscs into Neural Crest Using Top-Down Inhibition of Bmp Signaling. *Methods Mol. Biol.* **2019**, *1976*, 49–54.
- (34) Chambers, S. M.; Fasano, C. A.; Papapetrou, E. P.; Tomishima, M.; Sadelain, M.; Studer, L. Highly Efficient Neural Conversion of Human Es and Ips Cells by Dual Inhibition of Smad Signaling. *Nat. Biotechnol.* **2009**, *27*, 275–280.
- (35) Klim, J. R.; Williams, L. A.; Limone, F.; Guerra San Juan, I.; Davis-Dusenbery, B. N.; Mordes, D. A.; Burberry, A.; Steinbaugh, M. J.; Gamage, K. K.; Kirchner, R.; Moccia, R.; Cassel, S. H.; Chen, K.;

- Wainger, B. J.; Woolf, C. J.; Eggan, K. Als-Implicated Protein Tdp-43 Sustains Levels of Stmn2, a Mediator of Motor Neuron Growth and Repair. *Nat. Neurosci* **2019**, 22, 167–179.
- (36) Osterholm, C.; Barczyk, M. M.; Busse, M.; Gronning, M.; Reed, R. K.; Kusche-Gullberg, M. Mutation in the Heparan Sulfate Biosynthesis Enzyme Ext1 Influences Growth Factor Signaling and Fibroblast Interactions with the Extracellular Matrix. *J. Biol. Chem.* **2009**, 284, 34935–34943.
- (37) Kuo, W. J.; Digman, M. A.; Lander, A. D. Heparan Sulfate Acts as a Bone Morphogenetic Protein Coreceptor by Facilitating Ligand-Induced Receptor Hetero-Oligomerization. *Mol. Biol. Cell* **2010**, *21*, 4028–4041.
- (38) Bishop, J. R.; Schuksz, M.; Esko, J. D. Heparan Sulphate Proteoglycans Fine-Tune Mammalian Physiology. *Nature* **2007**, *446*, 1030–1037.
- (39) Symes, K.; Smith, E. M.; Mitsi, M.; Nugent, M. A. Sweet Cues: How Heparan Sulfate Modification of Fibronectin Enables Growth Factor Guided Migration of Embryonic Cells. *Cell Adh Migr* **2010**, *4*, 507–510.
- (40) Joannides, A. J.; Fiore-Heriche, C.; Battersby, A. A.; Athauda-Arachchi, P.; Bouhon, I. A.; Williams, L.; Westmore, K.; Kemp, P. J.; Compston, A.; Allen, N. D.; Chandran, S. A Scaleable and Defined System for Generating Neural Stem Cells from Human Embryonic Stem Cells. Stem Cells 2007, 25, 731–737.
- (41) Chambers, S. M.; Qi, Y.; Mica, Y.; Lee, G.; Zhang, X. J.; Niu, L.; Bilsland, J.; Cao, L.; Stevens, E.; Whiting, P.; Shi, S. H.; Studer, L. Combined Small-Molecule Inhibition Accelerates Developmental Timing and Converts Human Pluripotent Stem Cells into Nociceptors. *Nat. Biotechnol.* **2012**, *30*, 715–720.
- (42) Morrison, G. M.; Oikonomopoulou, I.; Migueles, R. P.; Soneji, S.; Livigni, A.; Enver, T.; Brickman, J. M. Anterior Definitive Endoderm from Escs Reveals a Role for Fgf Signaling. *Cell Stem Cell* **2008**, *3*, 402–415.
- (43) Maccarana, M.; Casu, B.; Lindahl, U. Minimal Sequence in Heparin/Heparan Sulfate Required for Binding of Basic Fibroblast Growth Factor. *J. Biol. Chem.* **1993**, *268*, 23898–23905.
- (44) Sugaya, N.; Habuchi, H.; Nagai, N.; Ashikari-Hada, S.; Kimata, K. 6-O-Sulfation of Heparan Sulfate Differentially Regulates Various Fibroblast Growth Factor-Dependent Signalings in Culture. *J. Biol. Chem.* **2008**, 283, 10366–10376.
- (45) Teixeira, F.; Vijaya Kumar, A.; Kumar Katakam, S.; Cocola, C.; Pelucchi, P.; Graf, M.; Kiesel, L.; Reinbold, R.; Pavao, M. S. G.; Greve, B.; Gotte, M. The Heparan Sulfate Sulfotransferases Hs2st1 and Hs3st2 Are Novel Regulators of Breast Cancer Stem-Cell Properties. Front Cell Dev Biol. 2020, 8, 559554.
- (46) Zhang, P.; Lu, H.; Peixoto, R. T.; Pines, M. K.; Ge, Y.; Oku, S.; Siddiqui, T. J.; Xie, Y.; Wu, W.; Archer-Hartmann, S.; Yoshida, K.; Tanaka, K. F.; Aricescu, A. R.; Azadi, P.; Gordon, M. D.; Sabatini, B. L.; Wong, R. O. L.; Craig, A. M. Heparan Sulfate Organizes Neuronal Synapses through Neurexin Partnerships. *Cell* **2018**, *174*, 1450.
- (47) Asano, S. M.; Gao, R.; Wassie, A. T.; Tillberg, P. W.; Chen, F.; Boyden, E. S. Expansion Microscopy: Protocols for Imaging Proteins and Rna in Cells and Tissues. *Curr. Protoc Cell Biol.* **2018**, *80*, e56.
- (48) Holley, R. J.; Pickford, C. E.; Rushton, G.; Lacaud, G.; Gallagher, J. T.; Kouskoff, V.; Merry, C. L. Influencing Hematopoietic Differentiation of Mouse Embryonic Stem Cells Using Soluble Heparin and Heparan Sulfate Saccharides. *J. Biol. Chem.* **2011**, 286, 6241–6252.

☐ Recommended by ACS

Mirror Image Mucins and Thio Mucins with Tunable Biodegradation

Victoria R. Kohout, Jessica R. Kramer, et al.

JULY 20, 2023

JOURNAL OF THE AMERICAN CHEMICAL SOCIETY

READ 🗹

Metabolic Glycan Labeling in Primary Neurons Enabled by Unnatural Sugars with No S-Glyco-Modification

Jiayu Sun, Xing Chen, et al.

MAY 30, 2023

ACS CHEMICAL BIOLOGY

READ 🗹

Dual-Action Heteromultivalent Glycopolymers Stringently Block and Arrest Influenza A Virus Infection *In Vitro* and *Ex Vivo*

Badri Parshad, Sumati Bhatia, et al.

MAY 23, 2023 NANO LETTERS

READ 🗹

High-Throughput Analysis Reveals miRNA Upregulating α -2,6-Sialic Acid through Direct miRNA-mRNA Interactions

Faezeh Jame-Chenarboo, Lara K. Mahal, et al.

NOVEMBER 09, 2022

ACS CENTRAL SCIENCE

READ 🗹

Get More Suggestions >